

# Constraining the astrophysics and cosmology from 21cm tomography using deep learning with the SKA

Sultan Hassan<sup>1,2,★†</sup>, Sambatra Andrianomena<sup>3,2</sup>, Caitlin Doughty<sup>1</sup>

<sup>1</sup> *Department of Astronomy, New Mexico State University, Las Cruces, NM 88003, USA*

<sup>2</sup> *University of the Western Cape, Bellville, Cape Town 7535, South Africa*

<sup>3</sup> *South African Radio Astronomy Observatory (SARAO), Black River Park, Observatory, Cape Town, 7925, South Africa*

Accepted XXX. Received YYY; in original form ZZZ

## ABSTRACT

Future Square Kilometre Array (SKA) surveys are expected to generate huge datasets of 21cm maps on cosmological scales from the Epoch of Reionization (EoR). We assess the viability of exploiting machine learning techniques, namely, convolutional neural networks (CNN), to simultaneously estimate the astrophysical and cosmological parameters from 21cm maps from semi-numerical simulations. We further convert the simulated 21cm maps into SKA-like mock maps using the detailed SKA antennae distribution, thermal noise and a recipe for foreground cleaning. We successfully design two CNN architectures (VGGNet-like and ResNet-like) that are both efficiently able to extract simultaneously three astrophysical parameters, namely the photon escape fraction ( $f_{\text{esc}}$ ), the ionizing emissivity power dependence on halo mass ( $C_{\text{ion}}$ ) and the ionizing emissivity redshift evolution index ( $D_{\text{ion}}$ ), and three cosmological parameters, namely the matter density parameter ( $\Omega_m$ ), the dimensionless Hubble constant ( $h$ ), and the matter fluctuation amplitude ( $\sigma_8$ ), from 21cm maps at several redshifts. With the presence of noise from SKA, our designed CNNs are still able to recover these astrophysical and cosmological parameters with great accuracy ( $R^2 > 90\%$ ), improving to  $R^2 > 95\%$  towards low redshift and low neutral fraction values. Our results show that future 21cm observations can play a key role to break degeneracy between models and tightly constrain the astrophysical and cosmological parameters.

**Key words:** dark ages, reionisation, first stars – methods: numerical – methods: statistical

## 1 INTRODUCTION

The last global phase transition in the Universe, known as the Epoch of Reionization (EoR), marks the time at which the first stars gradually reionized the Inter-Galactic Medium (IGM) and the Universe underwent from highly neutral-opaque to highly ionized-transparent state (for a review, see e.g. Loeb & Barkana 2001). This epoch captures a wealth of information that is important to understand different stages of galaxy formation and evolution.

Constraining the astrophysical and cosmological parameters have always been the focus for most of observational and theoretical studies. Several techniques have been developed to constrain the cosmological parameters (e.g. matter

density parameter  $\Omega_m$  and Hubble constant  $H_0$ ) such as using the Cosmic Microwave Background (CMB) anisotropies measurements (e.g. Hinshaw et al. 2013; Planck Collaboration et al. 2016), Sunyaev-Zel’dovich cluster surveys (e.g. Battye & Weller 2003), galaxy clusters in optical and X-ray bands (e.g. Moscardini et al. 2001), gamma ray burst X-ray afterglow light curves (e.g. Cardone et al. 2010), lensed GW+EM signals (e.g. Li et al. 2019), Ly- $\alpha$  forest power spectrum and COBE-DMR (e.g. Phillips et al. 2001), large-scale clustering of SDSS luminous red galaxies (e.g. Padmanabhan et al. 2007), and a joint CMB and weak lensing analysis (e.g. Contaldi et al. 2003). On the other hand, several works have attempted to constrain the astrophysical parameters (e.g. the photon escape fraction ( $f_{\text{esc}}$ ) and ionizing emissivity evolution ( $\dot{N}_{\text{ion}}$ )), using Ly- $\alpha$  forest measurements (e.g. Becker & Bolton 2013), Lyman continuum (LyC) radiation from local galaxies (e.g. Leitert et al. 2013),

★ E-mail: shassan@nmsu.edu

† Tombaugh Fellow

and inferred constraints by tuning different theoretical models to other measurements (e.g. [Mitra et al. 2015](#); [Finlator et al. 2015a](#)).

While all these methods show different levels of success to place constraints on various parameters, tighter constraints are expected to come from the EoR through measurements of the 21cm fluctuations on cosmological scales. With its strong dependence on the ionization and density fields, the 21cm signal carries a wealth of information that is important in order to understand early stages of galaxy formation and evolution. In this light, many radio interferometer experiments, such as the Low Frequency Array (LOFAR; [van Haarlem et al. 2013](#)), the Precision Array for Probing the Epoch of Reionization (PAPER; [Parsons et al. 2010](#)), the Murchison Wide field Array (MWA; [Bowman et al. 2013](#)), the Giant Metrewave Radio Telescope (MWA; [Paciga et al. 2011](#)), the Hydrogen Epoch of Reionization Array (HERA; [DeBoer et al. 2017](#)) and Square Kilometer Array (SKA; [Mellema et al. 2013](#)) are devoted to detecting reionization in the near future. These growing observational efforts require equivalent efforts in both the theoretical and statistical sides, in order to prepare for extracting all possible information and constrain the cosmological and astrophysical parameters from future 21cm surveys.

Several studies have already shown that combining the 21cm power spectrum with the Markov Chain Monte Carlo (MCMC) analysis is a powerful technique to obtain tighter constraints and break degeneracy between models (e.g. [Greig & Mesinger 2015](#); [Liu et al. 2016](#); [Pober et al. 2016](#); [Hassan et al. 2017](#); [Park et al. 2019](#)). Besides the power spectrum, future 21cm surveys, the SKA in particular, are also expected to generate huge imaging datasets for the 21cm fluctuations on large scales that will contain more information than the power spectrum. To efficiently use the 21cm information stored in the 2-dimensional 21cm maps, Convolutional Neural Networks (CNNs) have been a very successful deep learning tool to recover the astrophysical parameters during reionization ([Gillet et al. 2019](#)) and to identify reionization sources from different models ([Hassan et al. 2019](#)). However, the astrophysical parameter recovery by [Gillet et al. \(2019\)](#) ignores the instrumental effects as an initial proof-of-concept study. Accounting for these effects such as the angular resolution, foreground cleaning, and thermal noise, are all crucial in order to add some reality to the simulated 21cm images as we prepare for 21cm era.

In this work, we take a step further to design two different CNNs to simultaneously estimate several parameters from 21cm maps at several redshifts and different stages through reionization. Three astrophysical parameters are evaluated: the photon escape fraction ( $f_{\text{esc}}$ ), the ionizing emissivity power dependence on halo mass ( $C_{\text{ion}}$ ) and the redshift evolution index ( $D_{\text{ion}}$ ). Additionally, we estimate three cosmological parameters: the matter density parameter ( $\Omega_m$ ), the dimensionless Hubble constant ( $h$ ), and the matter fluctuation amplitude ( $\sigma_8$ ). To assess the ability of future 21cm tomography to constrain these parameters, we follow the recipe presented in [Hassan et al. \(2019\)](#) to add a physically motivated and realistic 21cm noise to large scale 21cm maps that are produced using our semi-numerical model, SIMFAST21 ([Santos et al. 2008, 2010](#)). This paper is organized as follows: we first describe our suite of simula-

tions of the 21cm signal and noise in §2. We then present the two network designs in §3 and the training dataset in §4. We present the main results in §5, and draw our concluding remarks in §6.

## 2 SIMULATIONS

### 2.1 Semi-Numerical Model, SIMFAST21

We use the Instantaneous model of our semi-numerical simulations SIMFAST21, that has been developed in [Hassan et al. \(2016\)](#), to improve over previous implementations of the ionizing source and sink populations in these semi-numerical simulations. In addition, it has been recently shown that this model is in a good agreement with predictions from our radiative transfer simulation (ARTIST; [Molaro et al. 2019](#)) in terms of the morphology and power spectrum of the ionization and 21cm fields. We here describe briefly the simulation ingredients, and defer to [Santos et al. \(2010\)](#) for the full details of the simulation algorithm, and to [Hassan et al. \(2016\)](#) for the Instantaneous model development.

The dark matter density is generated in the linear regime from a Gaussian distribution using a Monte-Carlo approach. Evolving the density field to non-linear regime is performed through the [Zel'dovich \(1970\)](#) approximation. Halos are then generated using the excursion-set formalism (ESF). Ionized regions are identified using a similar form of the ESF that is based on a direct comparison between the instantaneous rates of ionization  $R_{\text{ion}}$  and recombination  $R_{\text{rec}}$  in spherical regions of decreasing sizes as specified by the ESF. Regions are flagged as ionized if:

$$f_{\text{esc}} R_{\text{ion}} \geq R_{\text{rec}}, \quad (1)$$

where  $f_{\text{esc}}$  is the escape fraction. The  $R_{\text{rec}}$  is obtained from a radiative transfer simulation ([Finlator et al. 2015b](#)), in order to account for the clumping effects below our cell size. The  $R_{\text{rec}}$  is parameterized as a function of overdensity  $\Delta$  and redshift  $z$  as follows:

$$\frac{R_{\text{rec}}}{V} = 9.85 \times 10^{-24} (1+z)^{5.1} \left[ \frac{(\Delta/1.76)^{0.82}}{1 + (\Delta/1.76)^{0.82}} \right]^4, \quad (2)$$

where  $V$  refers to the cell volume. The  $R_{\text{ion}}$  parameterization is derived from a combination of the radiative transfer simulation ([Finlator et al. 2015b](#)), and a larger hydrodynamic simulation ([Davé et al. 2013](#)) that both have been shown to reproduce wide range of observations, including low- $z$  observations. The  $R_{\text{ion}}$  is parameterized as a function of halo mass  $M_h$  and redshift  $z$  as follows:

$$\frac{R_{\text{ion}}}{M_h} = 1.1 \times 10^{40} (1+z)^{D_{\text{ion}}} \left( \frac{M_h}{9.51 \times 10^7} \right)^{C_{\text{ion}}} \exp \left( \frac{-9.51 \times 10^7}{M_h} \right)^{3.0}, \quad (3)$$

where the best fit values of the ionizing emissivity dependence on halo mass  $C_{\text{ion}}$  and redshift  $D_{\text{ion}}$  were found to be  $C_{\text{ion}} = 0.41$  and  $D_{\text{ion}} = 2.28$ , respectively. Later, we will change these parameters to generate the training and testing datasets. Note that Equation (3) shows that  $R_{\text{ion}}$  scales as  $M_h^{1.41}$ , which is consistent with the SFR- $M_h$  relation previously found by [Finlator et al. \(2011\)](#). We defer to [Hassan et al. \(2016\)](#) for the full details on the derivation

Array design	866 compact core
Station diameter, $D$ [m]	35
Station area, $A$ [ $m^2$ ]	$962.11 \left( \frac{110}{\nu[\text{MHz}]} \right)^2$
system temperature [K] ( $= T_{\text{sky}} + T_{\text{rcvr}}$ )	$1.1 T_{\text{sky}} + 40$
Total observation time $t_{\text{int}}$ [h]	1000
Frequency resolution $\Delta\nu$ [kHz]	48
Redshift	10, 9, 8, 7
Frequency [MHz]	129, 142, 158, 178
FWHM [arcmin]	1.37, 1.24, 1.12, 0.99
Beam angle $\theta$ [rad]	0.066, 0.06, 0.054, 0.048
Default wedge slope $m$ , Equation. (4)	0.27, 0.23, 0.19, 0.15

**Table 1.** Summary of our assumed SKA array design.

of the  $R_{\text{ion}}$  and  $R_{\text{rec}}$  fitting functions and their effects on several reionization key observables.

## 2.2 21cm Instrument Simulation

We here describe the method used to account for various instrumental effects following the recipe developed in [Hassan et al. \(2019\)](#). We briefly review this method below and refer the interested readers to [Hassan et al. \(2019\)](#) for detailed information and complete steps of how we convert an 21cm simulated map into a *mock map* according to the assumed array design. In this work, we restrict our analysis to the SKA proposed design and leave a more detailed comparison between different arrays, such as HERA and LOFAR, for future works.

The 21cm Instrument simulation pipeline consists of three parts:

- **Angular resolution:** we account for the angular resolution of a given array by exploiting its detailed baseline distribution, via the  $uv$ -coverage, which is a measure of the baseline intensity observing the signal modes in directions perpendicular to the sightline. The  $uv$ -coverage is computed using the 21CMSENSE package<sup>1</sup> from our assumed SKA antennae distribution. We then Fourier transform the simulated 21cm map and set the signal to zero at  $k_{\perp}$  modes whose  $uv$ -coverage is zero<sup>2</sup>. We additionally smooth down the simulated maps using a Gaussian filter whose full width half maximum (FWHM) is given by:  $\text{FWHM} = \lambda_{21\text{cm}} (1+z)/B$ , whereas the maximum baseline length  $B=5,834$  m for our assumed SKA design, and  $\lambda_{21\text{cm}}$  is the rest frame wavelength of the 21cm signal. This sets the minimum angular resolution for our assumed SKA design. For instance, our simulated maps initially have an angular resolution of  $\sim 0.3'$  at  $z=7$ , that are smoothed to have a lower angular resolution of  $\sim 1'$  according to the FWHM at this redshift. Exact angular resolution values as a function of redshift are quoted in Table 1.

<sup>1</sup> <https://github.com/jpober/21cmSense>

<sup>2</sup> Modes with zero  $uv$ -coverage lie outside the angular resolution of the experiment.

- **Foreground cleaning:** Foreground contaminated modes of the signal lie inside the foreground wedge in the  $k_{\perp} - k_{\parallel}$  plane. The foreground wedge slope ( $m$ ) is given by:

$$m = \frac{D H_0 E(z) \sin \theta}{c(1+z)}, \quad (4)$$

where  $H_0$  is the Hubble parameter,  $c$  is the speed of light,  $E(z) \equiv \sqrt{\Omega_m(1+z)^3 + \Omega_{\Lambda}}$ , and  $\theta$  is the beam angle. To clean foregrounds, we simply zero out all modes within the wedge, satisfying  $k_{\parallel} < m k_{\perp}$ . For the same experiment, the slope increases with redshift, which means more modes are removed at higher redshifts. We quote exact wedge slope values for the SKA at our redshifts of interest in Table 1.

- **Thermal noise:** the thermal noise is uncorrelated between measurements, and can be drawn from a Gaussian distribution of unit mean and standard deviation ([Zaldarriaga et al. 2004](#)) given by:

$$\sqrt{\langle |N|^2 \rangle [\text{Jy}]} = \frac{2 k_B T_{\text{sys}}}{A \sqrt{\Delta\nu t_{\text{int}}}}, \quad (5)$$

where  $t_{\text{int}}$  here is the integration time to observe a single visibility at a frequency resolution  $\Delta\nu$ , and  $k_B$  is the Boltzmann constant. The total system temperature  $T_{\text{sys}}$  and other parameters are summarized in Table 1. Having generated the thermal noise in 2D grid using the above equation in Fourier space, we further suppress the noise by the amount of the  $uv$ -coverage  $N_{uv}$  by a factor of  $\sim 1/\sqrt{N_{uv}}$ . We finally inverse Fourier transform the noise map and add it to the angular resolution - foreground filtered signal map to form our mock 21cm map.

Using this pipeline with parameters listed in Table 1, the rms brightness temperature (noise level) is about  $\sim 3$  mK at  $z=8$ , consistent with previous estimates (e.g. see [Furlanetto et al. 2006](#); [Kakiichi et al. 2017](#); [Giri et al. 2018](#)). This pipeline is used to add some reality to our simulated training and testing dataset, in order to assess the ability of future SKA 21cm surveys to constrain the astrophysical and cosmological constraints. In Figure 1, we show an example of four randomly selected 21cm maps (top) with their mock versions (bottom) from our training dataset for different set of astrophysical and cosmological parameters as quoted in the subtitles. These maps are generated from different simulations realizations of a box size of  $L=150$  Mpc, number of cells  $N=200$ , resulting in a resolution of 0.75 Mpc. We find that most of the large and small scale ionized bubbles are still present after adding the instrumental effects. This is due to the high angular resolution of our assumed SKA design as well as the high  $uv$ -coverage that extends down to a very small scales ( $\sim 3.5$  h/Mpc) during these epochs. When the Universe is highly ionized (blue region), the noise dominates and the 21cm signal approaches zero, but nevertheless the signal features can still be seen and recognized. On the other hand, in the beginning of reionization, the ionized regions are very small due to the small number of sources and ionizing photons. The noise still contaminates these small ionized regions, which makes recognizing the prominent signal features more challenging, and many of the reionization realizations (e.g. with different seeds of the initial density perturbations) for a highly neutral Universe become approximately indistinguishable. This might impact the parameter recovery from a highly neutral IGM, which basically exists at high redshifts where the noise is stronger.

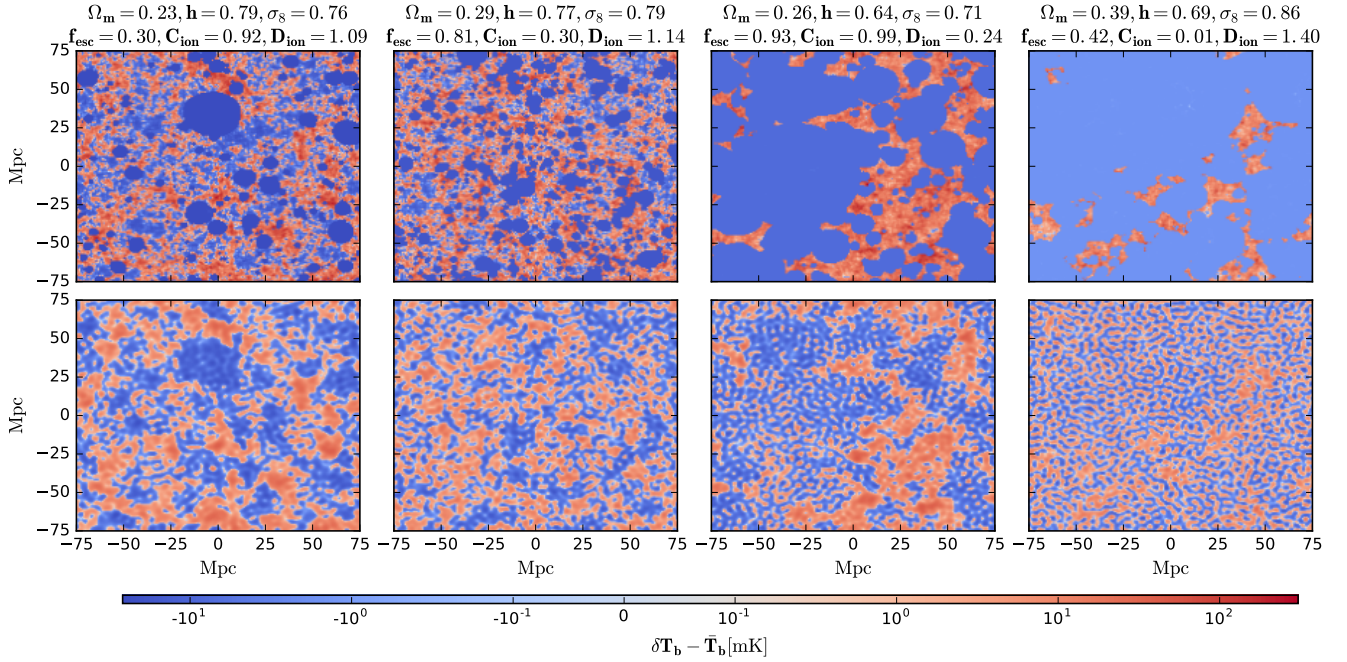


**Figure 1.** Examples of four randomly selected 21cm maps (top), from our training dataset, with their corresponding mock version (bottom), using our assumed SKA design. Subtitles show the astrophysical and cosmological parameters used to generated each map. These parameters are: the photon escape fraction ( $f_{esc}$ ), ionizing emissivity power dependence on halo mass ( $C_{ion}$ ) and ionizing emissivity redshift evolution index ( $D_{ion}$ ), matter density parameter ( $\Omega_m$ ), dimensionless Hubble constant ( $h$ ), and matter fluctuation amplitude ( $\sigma_8$ ).

### 3 NETWORK ARCHITECTURE

We consider two types of network in this work. It is worth reiterating that our main objective is to able to infer both astrophysical  $\{f_{esc}, C_{ion}, D_{ion}\}$  and cosmological  $\{\Omega_m, h, \sigma_8\}$  parameters simultaneously from their corresponding 21cm maps. To this end, our main focus is to simply explore different network designs with different layout in width and depth as an attempt to achieve our goal.

The first architecture (**network I**) considered for our investigation is given in Table. 2. It is slightly similar to VGG-Net (Simonyan & Zisserman 2014) in terms of chaining convolutional layers before downsampling, however the key difference here is that each stage<sup>3</sup>, we have two convolutional layers with same number of feature maps in a row followed by batch normalisation and ReLU activation (Conv+Conv+BN+ReLU) as shown in Figure 2. We note that the representation  $N \times N + M(S)$  denotes the kernel size ( $N \times N$ ) and the stride ( $M$ ) of a convolutional layer. In total, we have four stages, each with a Conv+Conv+BN+ReLU layer followed by a Max Pooling with stride = 2 to reduce the dimensions of the inputs<sup>4</sup>, and four dense layers each with 1024 units with the exception of the output layer, which has only 6 units corresponding to the number of inferred parameters. This network design is also similar to the previous design used in our reionization models classifier (Hassan

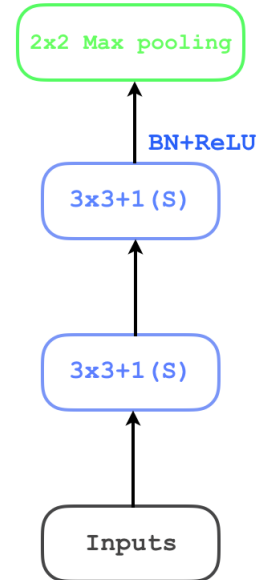


**Figure 2.** One stage in **network I**. Chaining two convolutional layers with same number of feature maps followed by a batch normalisation and ReLU function before a max pooling.

<sup>3</sup> which we refer to as mapping the input  $x$  without reducing the dimensions (weight  $\times$  height).

<sup>4</sup> In other words, the outputs from the previous stage.

et al. 2019), except that the convolutional layers used here are wider and no dropout seems to be needed. This is consistent with the disharmony observed between batch normalization and dropout (Li et al. 2018). Similar to our previous

**Table 2.** The architecture of **Network I** for this study.

Layer	Output shape
1	Input (1, 200, 200)
2	3×3 Convolutional Layer (32, 200, 200)
3	3×3 Convolutional Layer (32, 200, 200)
4	Batch Normalization –
5	ReLU Activation –
6	2×2 Max Pooling (32, 100, 100)
7	3×3 Convolutional Layer (64, 100, 100)
8	3×3 Convolutional Layer (64, 100, 100)
9	Batch Normalization –
10	ReLU Activation –
11	2×2 Max Pooling (64, 50, 50)
12	3×3 Convolutional Layer (128, 50, 50)
13	3×3 Convolutional Layer (128, 50, 50)
14	Batch Normalization –
15	ReLU Activation –
16	2×2 Max Pooling (128, 25, 25)
17	3×3 Convolutional Layer (256, 25, 25)
18	3×3 Convolutional Layer (256, 25, 25)
19	Batch Normalization –
20	ReLU Activation –
21	Fully Connected Layer (1024)
22	Batch Normalization –
23	ReLU Activation –
24	Fully Connected Layer (1024)
25	Batch Normalization –
26	ReLU Activation –
27	Fully Connected Layer (1024)
28	Batch Normalization –
29	ReLU Activation –
30	Fully Connected Layer (6)

works in the classifier, we initialize the network weights using a generalized form of Xavier initializer (Glorot & Bengio 2010) that is also called the Variance Scaling initializer, in which the random numbers are drawn from a zero mean Gaussian distribution whose variance is equal to the inverse of the average of the number of input and output neurons. This initializer ensures that the variance of the input data is preserved as it propagates through the network layers.

Our second architecture, which we simply name **network II**, is based on a combination of residual layers (He et al. 2016) and inception modules (Szegedy et al. 2015) as shown in Table. 3. The inputs, as described in §2, are first fed into a convolutional layer followed by a batch normalization (Ioffe & Szegedy 2015) before a ReLU activation (Conv+BN+ReLU). This is then followed by four residual layers, each composed of three, six, six and three residual blocks respectively. As shown by He et al. (2016), in order to mitigate the rather counter-intuitive worse performance of a deep network compared to that of a shallower one, they proposed a *residual mapping* instead of an *unreferenced mapping* according to

$$\mathcal{H}(\mathbf{x}) = \mathcal{F}(\mathbf{x}) + \mathbf{x}, \quad (6)$$

**Table 3.** The architecture of **Network II** for this study.

Layer	Output shape
1	Input (1, 200, 200)
2	Convolutional Layer (16, 200, 200)
3	Batch Normalization –
4	ReLU Activation –
5	Residual Layer (3 Residual Blocks) (16, 100, 100)
6	Residual Layer (6 Residual Blocks) (32, 50, 50)
7	Residual Layer (6 Residual Blocks) (64, 25, 25)
8	Residual Layer (3 Residual Blocks) (128, 13, 13)
9	Inception Module (240, 13, 13)
10	Max Pooling (240, 7, 7)
11	Inception Module (240, 7, 7)
12	Inception Module (256, 7, 7)
13	Inception Module (288, 7, 7)
14	Max Pooling (288, 4, 4)
15	Fully Connected Layer (1024)
16	Batch Normalization –
17	ReLU Activation –
18	Fully Connected Layer (1024)
19	Batch Normalization –
20	ReLU Activation –
21	Fully Connected Layer (1024)
22	Batch Normalization –
23	ReLU Activation –
24	Fully Connected Layer (6)

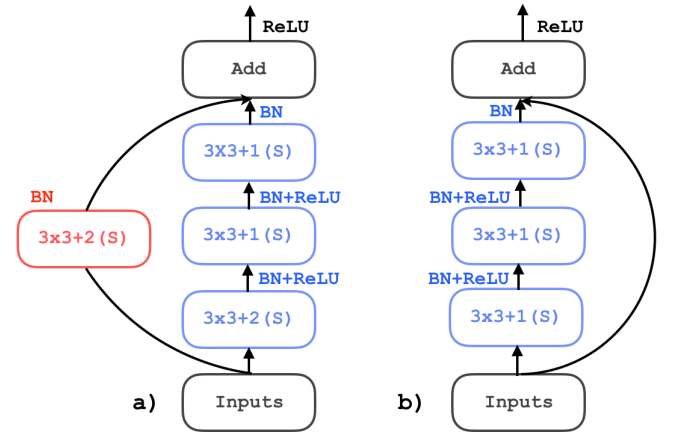


**Figure 3.** Residual block in Network II. *Left panel:* the downsampling only occurs at the first convolutional layer (blue 3×3+2(S)) but the dimension is kept the same at the second convolutional layer (blue 3×3+1(S)). The mapping  $\mathcal{W}(\mathbf{x})$  is done by using a convolutional layer (red 3×3+2(S)), such that the inputs and the residual  $\mathcal{F}(\mathbf{x})$  have the same dimensions. *Right panel:* when there is no downsampling, the inputs are simply added to  $\mathcal{F}(\mathbf{x})$  to construct the residual mapping.

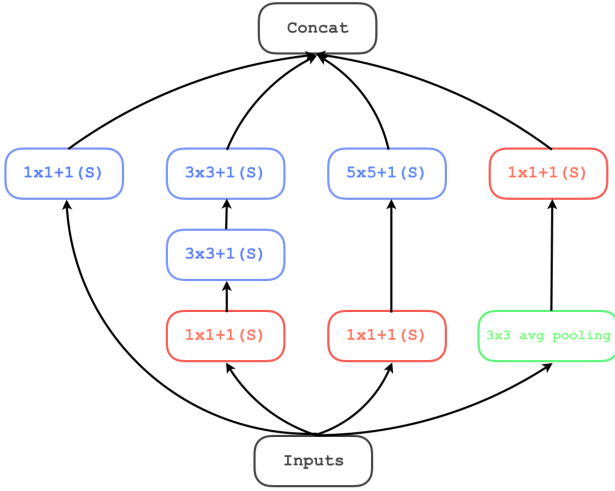


**Figure 4.** Inception module considered in this study. The red convolutional layers ( $1 \times 1(S)$ ) are used for dimensionality reduction.

where  $\mathcal{H}(\mathbf{x})$  is the original mapping and  $\mathcal{F}(\mathbf{x})$  is the residual. This is achieved with the schematic of a residual block shown in Figure. 3 (right panel) where the residual  $\mathcal{F}(\mathbf{x})$  is constructed using a Conv+BN+ReLU+Conv+BN+ReLU+Conv+BN layer. Depending on whether there is downsampling (Fig. 3 left panel), a mapping  $\mathcal{W}(\mathbf{x})$  – using a Conv+BN layer – is constructed in order to match the dimension of the output of  $\mathcal{F}(\mathbf{x})$  such that

$$\mathcal{H}(\mathbf{x}) = \mathcal{F}(\mathbf{x}) + \mathcal{W}(\mathbf{x}). \quad (7)$$

In each residual layer, the downsampling occurs at the first residual block. There are variants of deep residual networks, but in essence what we consider here is such that the network performance is optimized for our specific task. As proposed by Szegedy et al. (2015), in order to improve the recognition of more complex features at the higher levels of the network, we make use of four inception modules after the residual layers. The prescription suggested in Szegedy et al. (2015) is to deal with the computational complexity related to the depth of the network, *i.e.* increasing the size of the network while maintaining the computational cost. The inception module used in this network design is shown in Figure. 4. The idea behind convolving the inputs with a  $1 \times 1$  filter before the convolutional layers with  $3 \times 3$  and  $5 \times 5$  kernels is to reduce the number of feature maps from the inputs as computations are more expensive with larger kernel size. The features at different scales – captured by different kernel sizes  $1 \times 1$ ,  $3 \times 3$  and  $5 \times 5$  – can be learned *simultaneously* (Szegedy et al. 2015). It is worth noting that we opt for He initialization (He et al. 2016) for all layers in **network II**.

For training, as usual for any machine learning tasks, one needs to fine-tune the hyperparameters in order for the algorithm to generalize well and hence achieve the best possible performance, where the distance between the ground truth and network predictions is minimum. To that end, as shown in Table. 4, we use two completely different ap-

**Table 4.** The hyperparameters and optimisers used to train the algorithms.

	optimiser	learning rate	batch	cost function
<b>I</b>	Nesterov	0.005	128	$\ell_1$ norm
<b>II</b>	Adam	0.01	128	rmse

proaches in terms of optimisation for the two architectures. Although the two networks produce similar results, as will be presented in §5, **network I** converges faster. This can be explained by the capacity of **network I** with its number of trainable parameters of about 167 millions which translates to  $\sim 2.05 \times 10^9$  floating point operation per second (flops) at inference time, whereas **network II** has  $\sim 10$  millions of trainable parameters corresponding to  $\sim 1.39 \times 10^9$  flops at inference time.

#### 4 TRAINING DATASET

We generate the training dataset from a large simulation box of a size  $L=150$  Mpc with  $N=200^3$  cells. We run 1,000 different reionization simulations realizations with 1,000 different random seeds for the initial density field fluctuations. The prior range assumed to our parameters of interest is as follows:

- **Cosmology:**
  - Matter density parameter:  $0.2 \leq \Omega_m \leq 0.4$ .
  - Hubble constant:  $0.6 \leq h \leq 0.8$ .
  - Matter fluctuation amplitude:  $0.7 \leq \sigma_8 \leq 0.8$ .
- **Astrophysics:**
  - Photon escape fraction:  $0.01 \leq f_{\text{esc}} \leq 1$ .
  - $R_{\text{ion}}\text{-}M_{\text{h}}$  power dependence:  $0 \leq C_{\text{ion}} \leq 1$ .
  - $R_{\text{ion}}$  redshift evolution index:  $0 \leq D_{\text{ion}} \leq 2$ .

The range considered for the astrophysical parameters is motivated from our previous MCMC estimates to reproduce various reionization observables (Hassan et al. 2017), and those of the cosmology is inspired by the recent parameters estimates from the Planck Collaboration 2018 (Aghanim et al. 2018). From these priors, we select 1,000 values for each parameter using the Latin Hypercube Sampling (LHS) in order to efficiently explore our 6-dimensional parameter space and ensuring that the simulation doesn't run twice using the same set of parameters. We here account self-consistently for the cosmic variance in our training dataset since each map is originated from a different realization of the density field and produced by a different set of the astrophysical and cosmological parameters. From each simulation run, we store the 21cm brightness temperature at several redshifts  $z = 10, 9, 8, 7$  in order to have a sufficiently large number of maps to ensure training. We extract 76,300 21cm maps in total, and consider 80%, 10%, and 10% out of this total for training, testing and validation, respectively.

## 5 RESULTS

To assess how well the algorithms perform in terms of predicting the parameters from learning the input features, we use the coefficient of determination, also known as  $R^2$  score, which is given by

$$R^2 = 1 - \frac{\sum_{i=1}^n (y_i - \hat{y}_i)^2}{\sum_{i=1}^n (y_i - \bar{y})^2}, \quad (8)$$

where  $\hat{y}_i$ ,  $y_i$  and  $\bar{y}$  are the predicted value, the actual value and the average of all the actual values in the test sample respectively. The numerator of the second term in Equation 8 – residual sum of squares – quantifies the variation of the predicted values  $\hat{y}_i$  around the actual values  $y_i$ , and the denominator accounts for the variation of actual values  $y_i$  around their mean  $\bar{y}$ . This metric quantifies the strength of the correlation between the inferred and true values of the parameters, in other words unity  $R^2$  indicates that the network predictions are identical to the ground truth. The  $R^2$  also quantifies the fraction by which the predicted variance is less than the true variance. For each architecture, we carry out two types of training depending on the input features that the regressors are meant to learn from in order to infer our astrophysical and cosmological parameters ( $f_{\text{esc}}$ ,  $C_{\text{ion}}$ ,  $D_{\text{ion}}$ ,  $\Omega_m$ ,  $h$ ,  $\sigma_8$ ):

- feature extraction from a simulated 2D 21cm map (*clean/noiseless map* hereafter), this involves training and testing using *clean maps*
- feature extraction from a simulated 2D 21cm map which was convolved with a simulated SKA like noise (*noisy/mock map* hereafter, see §2), this consists of training and testing the networks using *noisy maps*.

### 5.1 Learning from *clean maps*

The top two rows in Figure 5 show the test results when training the networks with the *clean maps*. The red and blue areas are the predicted values of the parameters from **network I** and **network II** respectively. It is noted that the shaded areas represent  $1\sigma$  deviation obtained from binning the predictions around the mean of the true labels at each bin.

Overall, the constraints on each parameter are relatively tight as indicated by the relatively small deviations about the identity line (solid black). The high value of the  $R^2$  score ( $\geq 0.94$  for **network I** and  $\geq 0.96$  for **network II**) corresponding to each parameter fitting also denotes relatively strong correlation between the true and inferred parameter, suggesting that the algorithms are able to learn the salient features from the data. However, it appears that in general the cosmological parameters  $\{\Omega_m, h, \sigma_8\}$  are a bit more difficult to fit than the astrophysical ones  $\{f_{\text{esc}}, C_{\text{ion}}, D_{\text{ion}}\}$ . This might be due to the fact that the 21cm signal is more sensitive to the ionization state of the medium than to the underlying density field, which is controlled directly by the astrophysical parameters. The topology of the 21cm field is strongly affected by the ionized bubbles’ growth that is driven by changes in the reionizing photon source models, and hence the astrophysical parameters. The density field impact (cosmological parameters) is stronger and seen at small scales in the neutral regions, but weaker over these

large-scale maps where the prominent bubble features dominate. This indicates that these networks are using the ionized bubble sizes and distributions to create the mapping in the 6-dimensional space between the astrophysical and cosmological parameters, resulting in better constraints on the former compared to those on the latter.

On comparing the performance of the two architectures, their  $R^2$  score for each fitting suggests that they are in a fairly good agreement, and hence perform equally well despite the small discrepancies. For instance, **network I** constrains  $f_{\text{esc}}$  slightly better than **network II**, whereas the latter fits  $\Omega_m$  better than the former.

### 5.2 Learning from *noisy maps*

The test results after training the algorithms on the *noisy maps* are presented in the bottom two rows in Figure 5. The constraints on all parameters are weaker as compared to those obtained from training the fitters using the *clean maps*, as indicated by the larger  $1\sigma$  deviations (shaded areas). The overall decrease in performance denoted by the lower values of  $R^2$  score corroborates that finding. This can be accounted for by the fact that the relevant features are in this case convolved with noise, therefore extracting them is a bit more challenging.

The fact that the cosmological parameters are a bit harder to constrain is even more apparent when the maps considered for the training are contaminated by the instrumental effects. Despite being convolved with noise, which essentially causes the quality of their features to degrade, the maps are still more sensitive to the astrophysical parameters. Although a relatively poorer performance when extracting the relevant features from the *noisy maps*, the  $R^2$  scores, which are all  $\geq 0.79$  for **network I** and  $\geq 0.88$  for **network II**, suggest that the constraints on all parameters are still promising. In contrast to training the algorithms with the *clean maps*, it can be noticed that, overall, **network II** outperforms **network I**, as demonstrated by the  $R^2$  scores of the former, which are a bit higher than those of the latter on all parameters.

### 5.3 Dependence on redshift and neutral fraction

In real observations, both foreground contamination and the thermal noise become stronger with increasing redshift. One would then expect some form of dependence of the constraints on redshift. To investigate that possibility, we bin the maps according to their redshift in the test sample and do the predictions by considering each bin separately using the regressors trained with the *noisy maps*. The results presented in the left panel of Figure 6 suggest that the two methods do not always exhibit the same trend on the variation of  $R^2$  as a function of  $z$  for all parameters. For  $\Omega_m, h, \sigma_8$ , the resulting constraints from **network I** appear to be lowest at smaller  $z$ , reach a maximum around  $z = 8$  then decrease at higher redshift, whereas the  $R^2$  scores obtained from **network II** is at its peak at the lowest redshift bin then decreases towards higher  $z$ , except for  $h$ . However for the astrophysical parameters, in general the performance of both networks gets worse at higher redshift. While **network II** tends to have a slightly higher accuracy for each parameter as a function of redshift than **network I**, the dependence

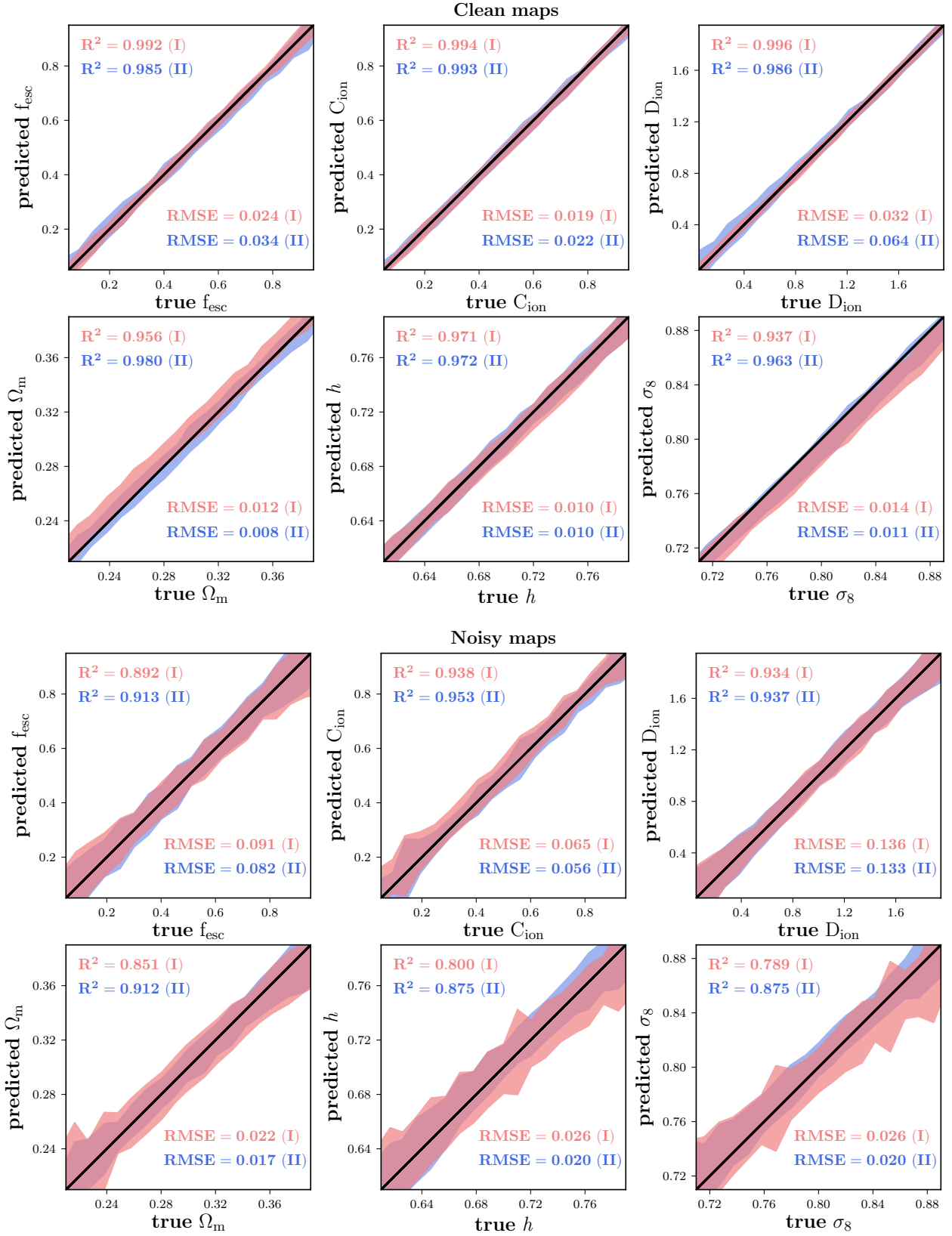


**Figure 5.** Correlation between the actual and predicted parameters. On the top two rows, the networks have been trained with the maps without noise, whereas on the bottom two rows, simulated SKA like noise has been injected into the maps which have been used to train the networks. Red and blue shaded areas are the predictions from **network I** and **network II** respectively. Solid black line represents the identity line *i.e.* true parameters vs true parameters. In all cases, the astrophysical parameters recovery is better than those of the cosmology. Adding the noise reduces the accuracy but the parameter recovery is still promising. The **network II** outperforms **network I**, particularly with the mock images, since more complex architecture seems to be needed to extract more information.



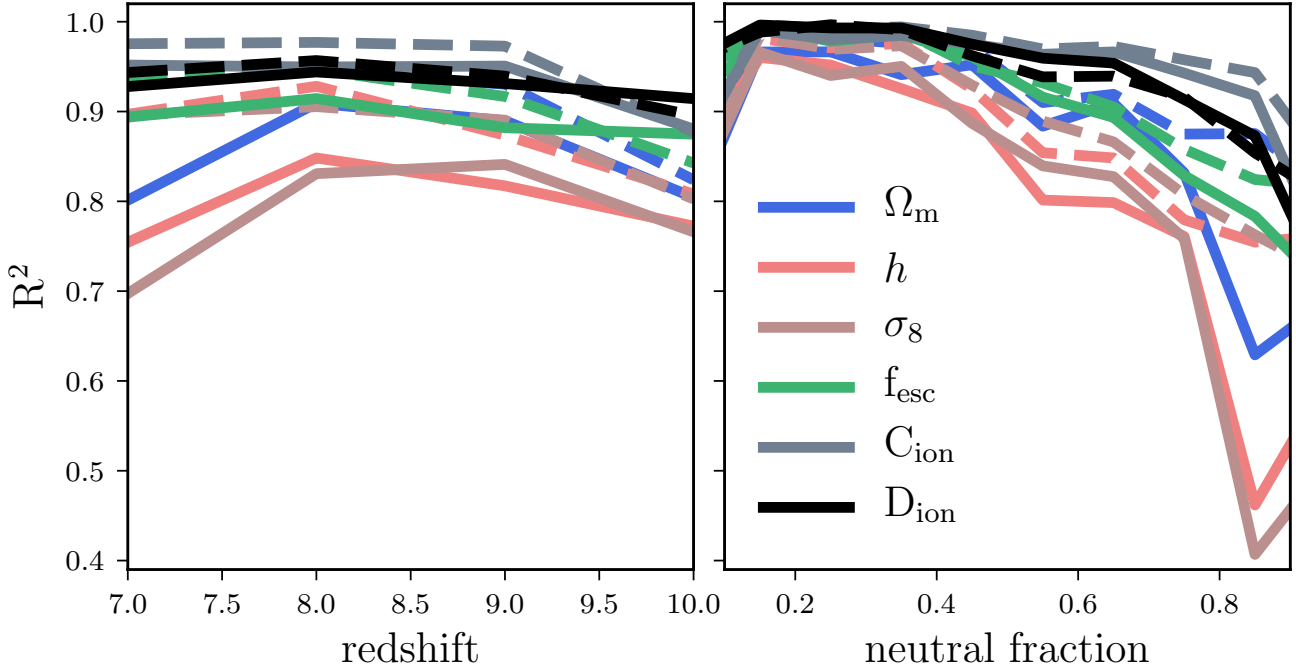


**Figure 6.** Variation of the resulting coefficient of determination  $R^2$  as a function of redshift (*left panel*) and neutral fraction (*right panel*). Solid and dashed lines correspond to **network I** and **network II** respectively. The accuracy of parameter recovery increases slowly towards low redshift, where the noise is smaller, and rapidly towards low neutral fraction values, where the images features can still be recognized (see Figure 1).

on redshift is fairly mild. This weak dependence is due to the fact that there are all possible neutral fraction values at each redshift, without imposing any prior knowledge to the training dataset by allowing certain neutral fraction values for each redshift, following the current reionization history constraints.

As mentioned and seen earlier, the observed features in a 21cm map are more dependent on  $x_{\text{HI}}$ . To address this effect on the performance of the algorithms, we now bin the slices according their value of  $x_{\text{HI}}$ . It is noticeable in Figure 6 right panel that the performance of each fitter on all parameters declines with increasing value of the neutral fraction. This is expected, as previously seen in Figure 1, the noise always dominates the ionized regions. When the Universe is highly ionized, the prominent features, which are probably the recombining clumps of the remaining dense gas, can still be seen in the presence of noise. This is in contrast to the case where the Universe is highly neutral, and the bubbles are small. Here, the ionized bubbles extend to much smaller scales where the noise dominates, and hence recognition of the bubbles becomes challenging. At this limit, different realizations (with different set of parameters) of a highly neutral Universe would look similar. This also explains the rapid increase of the accuracy of parameter recovery towards low neutral fraction values. Similar trends have been recently found with using deep learning to constrain the reionization history (Mangena et al. 2019).

Having established that the constraints are tighter at lower redshift and lower neutral fraction *i.e.* ionised case, we now apply some conditions on the test sample as follows

- select examples with  $x_{\text{HI}} < 0.5$ ,
- select examples with lower neutral fraction at lower redshift,  $x_{\text{HI}} < 0.5$  and  $z < 0.9$ .

We show in the top two rows of Figure 7 the resulting constraints on all parameters when considering maps with  $x_{\text{HI}} < 0.5$ . The results show how the constraints greatly improve by selecting examples with lower neutral fraction from the test sample. For this specific case, the coefficient of determination value  $\geq 0.91$  for **network I** and  $\geq 0.94$  for **network II** on all parameters indicates that the performance of the algorithms, despite considering *mock maps* for their training, is comparable to their performance when trained with *noiseless maps*.

Restricting ourselves to lower  $z$ , altogether with only selecting maps with low neutral fraction, in the test dataset further improves the predictions on all parameters as indicated by  $R^2 \geq 0.95$  for **network I** and  $R^2 \geq 0.97$  for **network II** (see Figure 7 bottom two rows). Inferring parameters from *noisy maps* at higher redshift is more challenging, since the noise is stronger (see Figure 6 left panel). Therefore one would expect further improvement of the predictions by combining the two criteria  $x_{\text{HI}} < 0.5$  and  $z < 0.9$ . This is an exciting result for future 21cm surveys that tighter constraints can be obtained by limiting the observations to lower redshifts ( $z \sim 6, 7$ ), where the Universe is highly Ionized. Using this technique, the SKA will be able to place their first constraints on the astrophysical and cosmological parameters in the near future and from the first cycle of imaging.

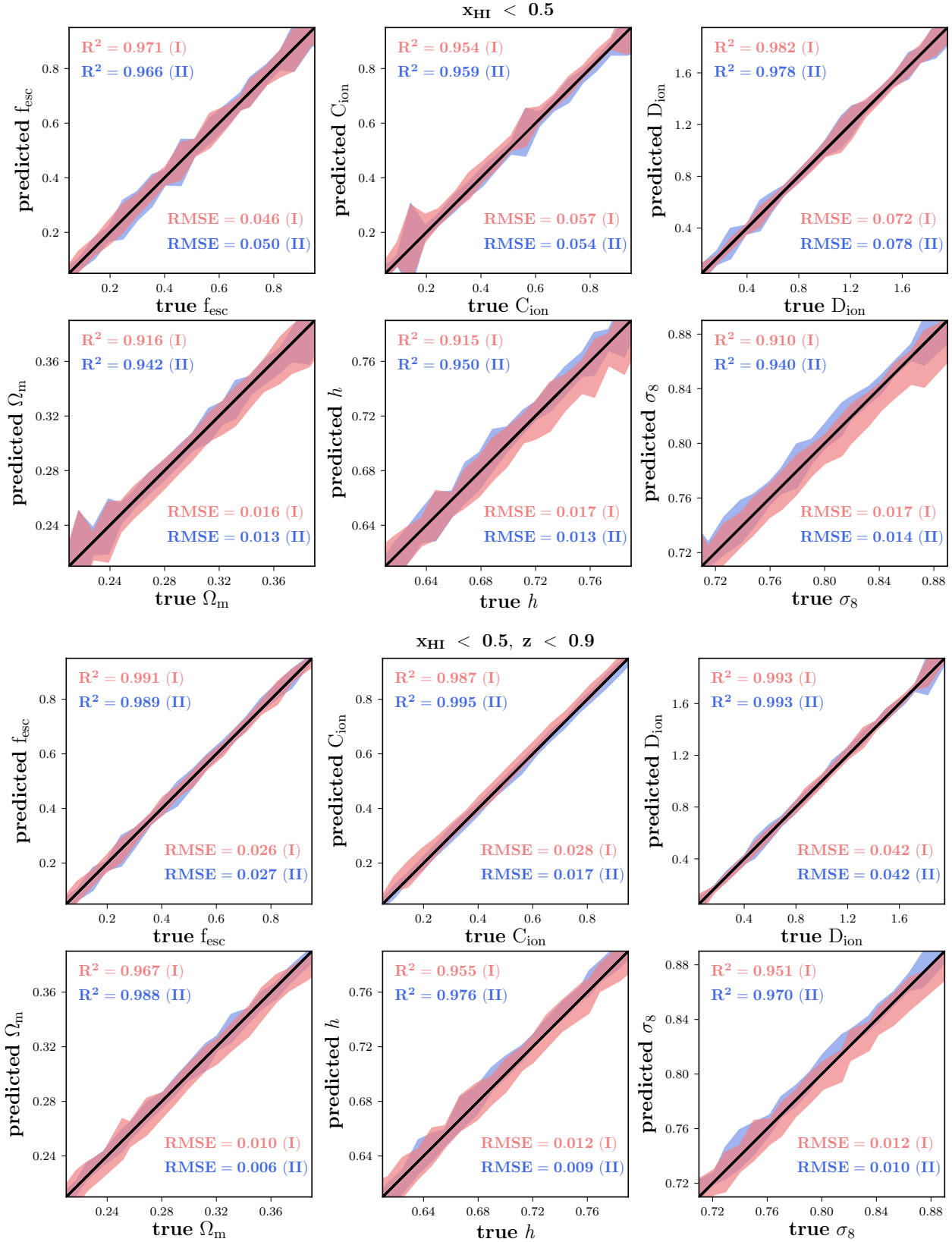


**Figure 7.** Correlation between the actual and the predicted parameters. On the top two rows, the networks have been trained with the *noisy maps* but a test sample with a neutral fraction  $< 0.5$  has been used for predictions. On the bottom two rows, the same *noisy* data have been used to train the networks but some cut on both the neutral fraction  $< 0.5$  and redshift  $z < 0.9$  have been applied on the test sample. Red and blue shaded areas are the predictions from **network I** and **network II** respectively. Solid black line represents the identity line *i.e.* true parameters vs true parameters. Imposing constraints on the neutral fraction and redshift of the testing sample increases the accuracy and performance is comparable to the case without including any instrumental effects as seen in top rows in Figure 5.

#### 5.4 Generalisation error

For the sake of completeness and in order to be able to compare our results to other similar studies, we compute, for each parameter, the resulting Root Mean Square Error, RMSE, as follows:

$$\text{RMSE} = \sqrt{\frac{1}{N} \sum (y_{\text{predicted}} - y_{\text{true}})^2}, \quad (9)$$

where as the summation runs through the whole test dataset. This metric, among others, tells us about the generalisation error inherent to our parameter estimation, in other words the level of accuracy<sup>5</sup> the fitters can achieve on average when estimating the parameters from encoding the inputs. We show the RMSE values obtained for each parameter when considering both *noiseless* and *noisy maps* in Figure 5 (two top rows and two bottom rows respectively). By comparing the RMSE values resulting from training on *clean maps* and those obtained from training on *mock maps*, we find that in the idealised scenario the prediction is subject to smaller average error for each parameter in contrast to the realistic one. This finding is expected and consistent with our results based on the  $R^2$  metric in that the inference is more challenging for each parameter when the data considered for training/testing are contaminated by noise. Although the results based on the two metrics are found to be consistent, it is tempting to expect that for any two different parameters, irrespective of the case (*noisy* or *clean maps*), if the  $R^2$  score of one of them is higher than that of the other, it implies that its RMSE must be lower. This does not hold since each parameter has its own dynamic range.

Gupta et al. (2018), by training a convolutional neural network with  $\sim 26$  millions parameters to predict cosmological parameters from simulated noiseless convergence maps, arrived at a generalisation error of  $35 \times 10^{-3}$  for  $\Omega_m$  and  $40.3 \times 10^{-3}$  for  $\sigma_8$ . Ribli et al. (2018) improved the constraints with a different neural network architecture of about  $\sim 1.4$  millions parameters, by also using simulated lensing maps, achieving  $\text{RMSE} = 5.5 \times 10^{-3}$ ,  $13.5 \times 10^{-3}$  for  $\Omega_m$  and  $\sigma_8$  respectively. In terms of encoding features from a 2D map using convolutional neural network to infer cosmological parameters, our results –  $\text{RMSE} = 11 \times 10^{-3}$  and  $8 \times 10^{-3}$  on  $\Omega_m$  from **network I** and **network II** respectively,  $\text{RMSE} = 14 \times 10^{-3}$ ,  $11 \times 10^{-3}$  on  $\sigma_8$  from **network I** and **network II** respectively – are comparable to those obtained in these previous works. More importantly, our results corresponding to the realistic case, with/without imposing constraints (see Figure 5 bottom row and Figure 7), where the input maps are *noisy* are very promising and exciting for future 21cm surveys.

## 6 CONCLUSIONS

We have demonstrated in this work the feasibility of inferring simultaneously both astrophysical and cosmological parameters ( $f_{\text{esc}}$ ,  $C_{\text{ion}}$ ,  $D_{\text{ion}}$ ,  $\Omega_m$ ,  $h$ ,  $\sigma_8$ ) using 21cm maps from the EoR, considering future HI surveys with the SKA. To this end, we have generated thousands of realizations each with

a different set of parameters using SIMFAST21 then compiled a dataset composed of 2D maps (see §4 for details). The approach is to train our two proposed algorithms – convolutional neural network based – to extract the features from the maps in order to predict the underlying astrophysical and cosmological parameters. We have considered an optimistic case where we train the networks with *noiseless* simulated maps and a real world mimicking scenario in which the networks are trained with simulated maps contaminated by simulated SKA-like noise. We have used  $R^2$  – coefficient of determination – as a performance metric.

We summarize our findings as follows:

- The overall results for the idealised case, with  $R^2 \geq 0.94$  for **network I** and  $R^2 \geq 0.96$  for **network II** on all parameters, suggest that the algorithms considered in this work are capable of learning the salient features from the maps in order to constrain with a relatively good accuracy the corresponding parameters. It has been noticed that in general the astrophysical parameters are better constrained than the cosmological ones, owing to the fact that the topology of 21cm maps is strongly dependent on the ionized bubbles which in turn are conditioned by the astrophysical parameters and exploited by the regressors to build the mapping between the inputs and the output parameters.

- In a more realistic setup, where maps from observations are subject to noise contamination, the constraints on all parameters are relatively weaker. This is expected since disentangling the relevant information from noise is more challenging. It has been found that **network II**, leveraging the combination of residual layers at lower level and inception module at higher level of the architecture, outperforms **network I** despite the former's lower capacity. This then points towards deploying **network II** in a real world scenario.

- In the case of learning from the *noisy maps*, the predictions are dependent on both the underlying neutral fraction of the map and its distance from an observer. The performance of the methods improves with decreasing neutral fraction and, as foreground contamination is more important at higher redshift, the constraints are tighter at lower  $z$ . The results obtained from the test sample is  $R^2 \geq 0.91$  with **network I** and  $R^2 \geq 0.94$  with **network II** when only selecting maps with  $x_{\text{HI}} < 0.5$ . Recovery improves with imposing constraints on both neutral fraction and redshift ( $x_{\text{HI}} < 0.5$  at lower  $z < 0.9$ ), resulting in  $R^2 > 0.95$  with **network I** and  $R^2 > 0.97$  with **network II**. This indicates that even in the presence of *noise* in maps, our methods can still estimate the relevant parameters to a relatively good level of precision, which is indeed quite promising.

- We have computed the prediction error on average – RMSE – on each parameter in both optimistic and realistic cases. It has been found that the RMSE is smaller in the former, in good agreement with the results based on the choosing the coefficient of determination as a performance metric. Compared to other previous works, our approach has also shown a great potential for inferring the underlying parameters of what is observed in future cosmological experiments, such as HI intensity mapping.

Our results are entirely limited to the set of assumptions and approximation implemented in our 21cm instrument simulation. A more refined and sophisticated recipe to ac-

<sup>5</sup> Not to be confused with accuracy, the metric used in classification tasks.

count for all of the implemented instrumental effects, such as the angular resolution, foreground cleaning and thermal noise, might alter our concluding remarks. The approximation and assumptions implemented in the semi-numerical simulations, through the use of the excursion set formalism to identify the ionized regions, as well as the choice of our dynamic range and resolution, place additional limitations to the presented results. While limited to the SKA, our analysis can be easily extended to include instrumental effects from other 21cm surveys such as HERA and LOFAR, which we leave for future works to perform a detailed comparison between different array designs and different observing strategies. Inferring parameters from the 3D light cones might improve recovery in the presence of noise without the need to impose constraints on the neutral fraction or redshift. Our analysis also can be easily extended to include all of the astrophysical parameters from the source and sink models, and all cosmological parameters, which we leave for future works.

This study has not only highlighted the constraining power of our methods, probing deep into EoR in the near future with the arrival of more advanced HI instruments like SKA, but also shown how future 21cm surveys and HI intensity mapping can help break the degeneracy between models by combining them with other experiments, such as *Planck*, to better the constraints on cosmological parameters in an era of precision cosmology.

## ACKNOWLEDGEMENTS

The authors acknowledge helpful discussions with Laura Boucheron, Kristian Finlator, Jon Holtzman, Tumelo Mangena, James McAteer, Mario Santos, Rene Walterbos. Simulations and analysis were performed at UWC's PUMBAA, IDIA/ILFU cloud computing facilities, and NMSU's DISCOVERY supercomputers. This work also used the Extreme Science and Engineering Discovery Environment (XSEDE), which is supported by National Science Foundation grant number ACI-1548562, and computational resources (Bridges) provided through the allocation AST190003P. SA acknowledges financial support from the *South African Radio Astronomy Observatory* (SARAO) and is grateful to Sean February and Martin Slabber from the *Science Data Processing* (SDP) team at SARAO for their strong technical support with regards to the computing resources. CCD thanks the LSSTC Data Science Fellowship Program, which is funded by LSSTC, NSF Cybertraining Grant #1829740, the Brinson Foundation, and the Moore Foundation; Her participation in the program has benefited this work. CCD acknowledges funding from the New Mexico Space Grant Consortium Grant #NNX15AL51H.

## REFERENCES

Aghanim N., et al., 2018, arXiv preprint arXiv:1807.06209  
 Battye R. A., Weller J., 2003, *Phys. Rev. D*, 68, 083506  
 Becker G. D., Bolton J. S., 2013, *Monthly Notices of the Royal Astronomical Society*, 436, 1023  
 Bowman J. D., et al., 2013, *Publ. Astron. Soc. Australia*, 30, e031  
 Cardone V. F., Dainotti M. G., Capozziello S., Willingale R.,

2010, *Monthly Notices of the Royal Astronomical Society*, 408, 1181  
 Contaldi C. R., Hoekstra H., Lewis A., 2003, *Phys. Rev. Lett.*, 90, 221303  
 Davé R., Katz N., Oppenheimer B. D., Kollmeier J. A., Weinberg D. H., 2013, *MNRAS*, 434, 2645  
 DeBoer D. R., et al., 2017, *PASP*, 129, 045001  
 Finlator K., Davé R., Özel F., 2011, *ApJ*, 743, 169  
 Finlator K., Thompson R., Huang S., Davé R., Zackrisson E., Oppenheimer B. D., 2015a, *Monthly Notices of the Royal Astronomical Society*, 447, 2526  
 Finlator K., Thompson R., Huang S., Davé R., Zackrisson E., Oppenheimer B. D., 2015b, *MNRAS*, 447, 2526  
 Furlanetto S. R., Oh S. P., Briggs F. H., 2006, *Phys. Rep.*, 433, 181  
 Gillet N., Mesinger A., Greig B., Liu A., Ucci G., 2019, *MNRAS*, 484, 282  
 Giri S. K., Mellema G., Ghara R., 2018, *MNRAS*, 479, 5596  
 Glorot X., Bengio Y., 2010, in Proceedings of the thirteenth international conference on artificial intelligence and statistics. pp 249–256  
 Greig B., Mesinger A., 2015, *Monthly Notices of the Royal Astronomical Society*, 449, 4246  
 Gupta A., Matilla J. M. Z., Hsu D., Haiman Z., 2018, *Physical Review D*, 97, 103515  
 Hassan S., Davé R., Finlator K., Santos M. G., 2016, *MNRAS*, 457, 1550  
 Hassan S., Davé R., Finlator K., Santos M. G., 2017, *MNRAS*, 468, 122  
 Hassan S., Liu A., Kohn S., La Plante P., 2019, *MNRAS*, 483, 2524  
 He K., Zhang X., Ren S., Sun J., 2016, in Proceedings of the IEEE conference on computer vision and pattern recognition. pp 770–778  
 Hinshaw G., et al., 2013, *The Astrophysical Journal Supplement Series*, 208, 19  
 Ioffe S., Szegedy C., 2015, arXiv preprint arXiv:1502.03167  
 Kakiichi K., et al., 2017, *MNRAS*, 471, 1936  
 Leitert E., Bergvall N., Hayes M., Linné S., Zackrisson E., 2013, *A&A*, 553, A106  
 Li X., Chen S., Hu X., Yang J., 2018, arXiv e-prints, p. arXiv:1801.05134  
 Li Y., Fan X., Gou L., 2019, *The Astrophysical Journal*, 873, 37  
 Liu A., Pritchard J. R., Allison R., Parsons A. R., Seljak U., Sherwin B. D., 2016, *Phys. Rev. D*, 93, 043013  
 Loeb A., Barkana R., 2001, *Annual Review of Astronomy and Astrophysics*, 39, 19  
 Mangena T., Hassan S., MG S., 2019, submitted to MNRAS  
 Mellema G., et al., 2013, *Experimental Astronomy*, 36, 235  
 Mitra S., Choudhury T. R., Ferrara A., 2015, *Monthly Notices of the Royal Astronomical Society: Letters*, 454, L76  
 Molaro M., Davé R., Hassan S., Santos M. G., Finlator K., 2019, arXiv e-prints, p. arXiv:1901.03340  
 Moscardini L., Matarrese S., Mo H., 2001, *Monthly Notices of the Royal Astronomical Society*, 327, 422  
 Paciga G., et al., 2011, *MNRAS*, 413, 1174  
 Padmanabhan N., et al., 2007, *Monthly Notices of the Royal Astronomical Society*, 378, 852  
 Park J., Mesinger A., Greig B., Gillet N., 2019, *MNRAS*, 484, 933  
 Parsons A. R., et al., 2010, *AJ*, 139, 1468  
 Phillips J., Weinberg D. H., Croft R. A. C., Hernquist L., Katz N., Pettini M., 2001, *The Astrophysical Journal*, 560, 15  
 Planck Collaboration et al., 2016, *A&A*, 594, A13  
 Pober J. C., Greig B., Mesinger A., 2016, *MNRAS*, 463, L56  
 Ribli D., Pataki B. Á., Csabai I., 2018, arXiv preprint arXiv:1806.05995  
 Santos M. G., Amblard A., Pritchard J., Trac H., Cen R., Cooray A., 2008, *The Astrophysical Journal*, 689, 1

- Santos M., Ferramacho L., Silva M., Amblard A., Cooray A., 2010, *Monthly Notices of the Royal Astronomical Society*, 406, 2421
- Simonyan K., Zisserman A., 2014, arXiv preprint arXiv:1409.1556
- Szegedy C., et al., 2015, in *Proceedings of the IEEE conference on computer vision and pattern recognition*, pp 1–9
- Zaldarriaga M., Furlanetto S. R., Hernquist L., 2004, *ApJ*, 608, 622
- Zel'dovich Y. B., 1970, *A&A*, 5, 84
- van Haarlem M. P., et al., 2013, *A&A*, 556, A2